

## Combining incoherent scatter radar data and IRI-2007 to monitor the open-closed field line boundary during substorms

E. E. Woodfield,<sup>1</sup> J. A. Wild,<sup>1</sup> A. J. Kavanagh,<sup>1</sup> A. Senior,<sup>1</sup> and S. E. Milan<sup>2</sup>

Received 31 May 2010; revised 29 September 2010; accepted 6 October 2010; published 21 December 2010.

[1] The size of the polar cap is very important for understanding the substorm process as well as reconnection rates in general. In this work we build on previous studies which use a combination of European Incoherent Scatter radar (EISCAT) electron temperature ( $T_e$ ) measurements from two radars running simultaneously to track the motion of the open-closed field line boundary (OCB). The second radar gives an estimate of the background variation of  $T_e$  with altitude, which can then be subtracted from the radar beam being used to estimate the OCB location. We demonstrate that using the international reference ionosphere 2007 (IRI-2007) model can remove the second radar requirement and therefore increase the number of cases which could benefit from background  $T_e$  subtraction. In this paper we focus our analysis on substorm intervals. We find that the IRI-2007 method produces an OCB proxy location which on average is  $0.25^\circ$  altitude adjusted corrected geomagnetic coordinate latitude equatorward of the two-radar method. On comparing both the two-radar and IRI-2007  $T_e$  OCB finding methods with the OCB identified in the DMSP particle data and IMAGE satellite data we find that both EISCAT methods perform quite well, and neither method is particularly favored over the other. We find that the magnitude of the mean offset to the IMAGE OCB varies between  $0.1^\circ$  and  $2.7^\circ$  latitude, dependent on the event and the IMAGE camera used.

**Citation:** Woodfield, E. E., J. A. Wild, A. J. Kavanagh, A. Senior, and S. E. Milan (2010), Combining incoherent scatter radar data and IRI-2007 to monitor the open-closed field line boundary during substorms, *J. Geophys. Res.*, *115*, A00115, doi:10.1029/2010JA015751.

### 1. Introduction

[2] The size of the polar cap and hence the amount of open magnetic flux contained within it is a very important quantity when it comes to understanding the substorm process as well as reconnection rates in general (see, e.g., the review by *Chisham et al.* [2008]). The amount of open flux is determined by the rate of dayside reconnection, opening magnetic flux, and the nightside reconnection rate, closing flux in the magnetotail. Thus it is a measure of how energy is transferred through the Earth's magnetosphere. A great deal of scientific endeavor has gone into finding a good experimental method to locate the open-closed field line boundary (OCB) in recent years, as a result of which there are several different methods that can be used.

[3] Unfortunately, a totally reliable, continuous and global method of locating the OCB does not exist although many reasonable attempts can be made. Usually the most effective method is to combine several different proxies for the OCB with their associated advantages and disadvantages [e.g., *Wild et al.*, 2004]. Proxies which have been used previously

include: particle boundaries from DMSP satellites [*Newell et al.*, 1996] (usually considered to be the most accurate proxy), auroral observations from the ground [e.g., *Blanchard et al.*, 1995], auroral observations from space [e.g., *Boakes et al.*, 2008], spectral width boundaries from the SuperDARN (Super Dual Auroral Radar Network) coherent scatter radars [e.g., *Woodfield et al.*, 2002; *Chisham et al.*, 2005] and various signatures from incoherent scatter radars (electron density [*de la Beaujardière et al.*, 1991; *Blanchard et al.*, 1997], electron temperature [*Østgaard et al.*, 2005; *Aikio et al.*, 2006], and characteristic energy [*Doe et al.*, 1997]). A good explanation of these proxies and further references can be found in the review by *Chisham et al.* [2008], while *Doe et al.* [1997] gives a good description of the earlier incoherent scatter OCB proxies (density and characteristic energy).

[4] Incoherent scatter radars provide several different means to estimate the location of the OCB as mentioned above. In recent times the electron temperature ( $T_e$ ) has been used successfully by various authors [*Østgaard et al.*, 2005; *Aikio et al.*, 2006, 2008; *Hubert et al.*, 2010]. This method relies on the increase in electron temperature caused by auroral precipitation within the auroral oval. *Aikio et al.* [2006] refined the basic  $T_e$  method for the European Incoherent Scatter radar (EISCAT) system by subtracting an estimate of the background  $T_e$  dependence on altitude derived from the EISCAT Svalbard Radar (ESR) within the

<sup>1</sup>Physics Department, Lancaster University, Lancaster, UK.

<sup>2</sup>Department of Physics and Astronomy, University of Leicester, Leicester, UK.

polar cap. This gives a better indication of the  $T_e$  change with latitude since the height-dependent part of the  $T_e$  profile has been removed. There is an inherent difficulty with this particular method, namely the requirement to have two incoherent scatter radars running simultaneously in the necessary modes with minimal longitudinal separation. In operational terms this means that the ESR field aligned beam needs to be running at the same time as the low-elevation mode beam from the mainland EISCAT VHF system and/or the ESR steerable dish in low-elevation mode pointing equatorward. It would be very beneficial in terms of the number of experimental intervals both past and future when this kind of method could be used if an ionospheric model could be used to replace the need for the ESR field aligned beam to be running. This would increase the number of EISCAT experiments where this method could be used and also potentially extend the method to other radar systems which do not have a second radar in the polar cap.

[5] The international reference ionosphere 2007 (IRI-2007) model [Bilitza and Reinisch, 2008] may be able to provide a sufficiently good background  $T_e$  height profile. In this paper we assess the capabilities of the IRI-2007 model as a background height profile for  $T_e$  for finding the  $T_e$  boundary as compared to the method of Aikio *et al.* [2006, 2008]. We compare both the Aikio and IRI methods with particle precipitation boundaries from DMSP [Newell *et al.*, 1996] and the UV auroral imaging boundary from IMAGE [Boakes *et al.*, 2008]. We focus particularly on substorm intervals to assess the capabilities of the method for this phenomenon where knowledge of the OCB location is especially important.

## 2. Method

### 2.1. Choice of Cases

[6] The work of Aikio *et al.* [2006, 2008] concentrated on substorm times, a particularly useful time to know the location of the OCB and hence the area of the polar cap. We have continued this theme and have narrowed our testing to substorm periods. We have identified a subset of the extended Frey *et al.* [2004] list of substorms which has both EISCAT mainland and EISCAT Svalbard (ESR) data as well as DMSP nightside boundary identifications within  $\pm 15^\circ$  geographic longitude and  $\pm 30$  min of substorm onset.

[7] All the low-elevation EISCAT radar data in this paper comes from the VHF system based at Tromsø, Norway ( $69.59^\circ\text{N}$ ,  $19.22^\circ\text{E}$  geographic); however, these methods can equally well be used on low-elevation southward pointing data from the ESR. We have defined low elevation for our purposes as anything under  $40^\circ$ .

[8] An important caveat for both the Aikio and IRI OCB finding methods compared here is that the results are restricted to the latitude region covered by the low-elevation beam. In the case of VHF data this is approximately  $69^\circ$  to  $75^\circ$  altitude adjusted corrected geomagnetic (AACGM) latitude [Baker and Wing, 1989].

### 2.2. EISCAT and ESR $T_e$ Method

[9] The work of Aikio *et al.* [2006, 2008] improved upon the  $T_e$  OCB proxy method of Østgaard *et al.* [2005]. The Aikio method is a refinement of the idea that  $T_e$  measurements indicate the edge of the polar cap [e.g., Doe *et al.*,

1997]. The initial assumption is that the precipitation of particles within the auroral oval, equatorward of the polar cap, significantly raises  $T_e$ . Therefore a radar beam covering a range of latitudes can observe the poleward edge of the auroral oval and hence the OCB; however, the radar beam simultaneously covers a range of altitudes so it will also measure changes in  $T_e$  due to height. In the papers by Aikio *et al.* [2006, 2008] the background dependence of temperature on altitude in the polar cap is removed from the identification thus improving the technique. It is assumed that the nonauroral  $T_e$  height profile from the polar cap is applicable as a background for the auroral region. To achieve this the background  $T_e$  height profile from the polar cap (as determined by the ESR 42 m field-aligned data from Svalbard) is subtracted from the  $T_e$  measurements taken by the mainland EISCAT radar [see Aikio *et al.*, 2006, Figure 1]. This method will only work if the ESR (at Longyearbyen  $78.15^\circ\text{N}$ ,  $16.03^\circ\text{E}$  geographic) is located within the polar cap.

[10] The ESR method used here differs from the original Aikio method primarily in the algorithm we use to find the  $T_e$  OCB boundary, denoted here as  $bT_e$ , but we have also used a more broad brush approach to the ESR data processing so that detailed reanalysis of the ESR data (changing integration times etc.) is not required. Our aim is to produce a method that could be widely used by non-EISCAT experts so we have sourced all of our data from the easily accessible Madrigal database (available through the main EISCAT Web site <http://www.eiscat.se/madrigal>). As the results in section 3 show, this simplification does not have a particularly adverse effect on the outcomes.

### 2.3. IRI-2007 Method

[11] The IRI-2007 model [Bilitza and Reinisch, 2008] is a model of the ionosphere which provides monthly averages of various ionospheric parameters. It is an empirical model making use of data from ionosondes, incoherent scatter radars, topside sounders and in situ satellite and rocket instruments. The standard options were used in the model runs we performed; for details of the  $T_e$  models used, the reader is referred to Bilitza and Reinisch [2008, and references therein].

[12] We can use the IRI-2007 output as a substitute for the ESR data and thus both increase the number of cases where this method could be applied (because the requirement to have both the mainland and ESR radars systems running in the necessary configuration is reduced to just one radar system), and also potentially extend its use to other incoherent scatter radars.

### 2.4. Locating the OCB Proxy

[13] In the IRI method we use the IRI-2007 model to calculate a vertical profile of  $T_e$  in the polar cap at the latitude and longitude of the ESR radar. In using the IRI-2007 model one loses the benefit of contemporaneous observations which can take into account current conditions; however, it has the advantage of being available at all times unlike the ESR radar data. An example of the background produced in this way is shown in Figure 1a for the case on 29 October 2004. Whichever background method is used, the  $T_e$  height profile is then subtracted from the VHF data to give  $\Delta T_e$ .

[14] In the ESR method we evaluate the distribution of  $T_e$  at each range gate of the ESR field-aligned beam over a 30 min period centered on each VHF data point time. We

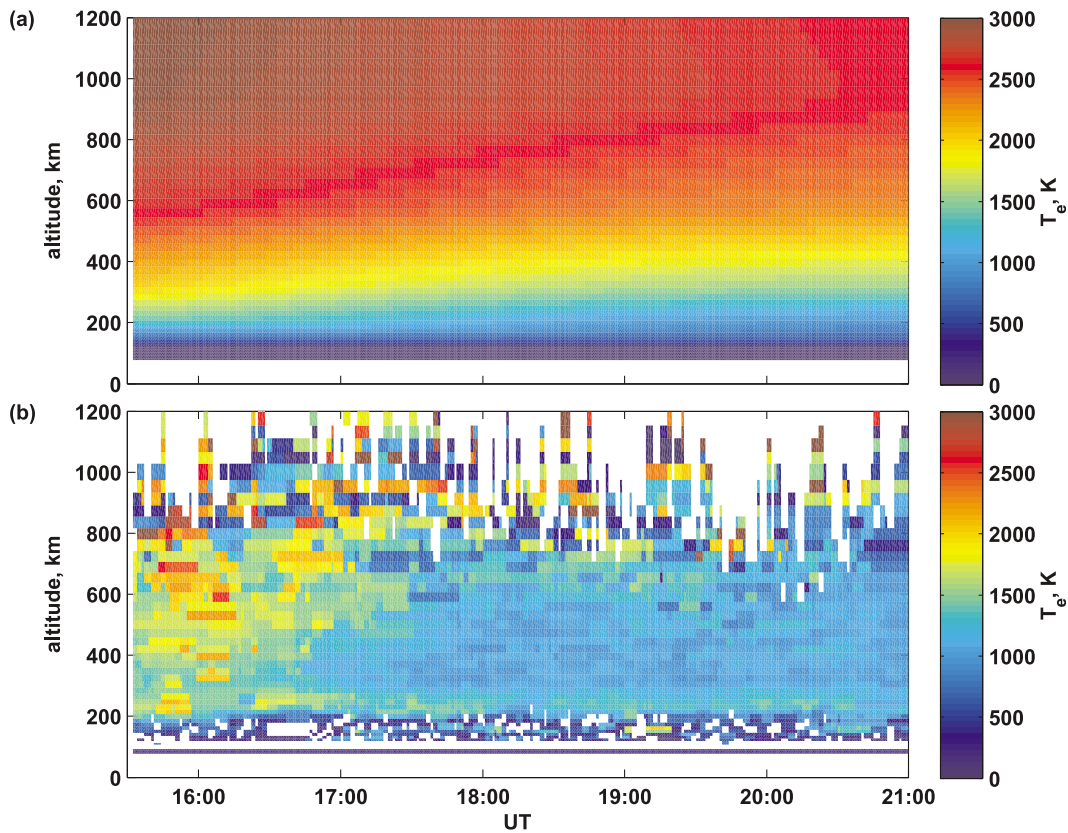


**Figure 1.** Background  $T_e$  from 29 October 2004 calculated with (a) IRI-2007 and (b) ESR.

then use the mode of this distribution at each height as a representation of the background  $T_e$  height profile. The mode proved more robust to large fluctuations in the data than using the mean in the cases we have used. This height profile from the polar cap is then assumed to be applicable as a background level over the whole range of latitudes covered by the VHF low-elevation beam. An example of the background produced from the ESR is shown in Figure 1b for comparison to the  $T_e$  from IRI-2007. As expected the ESR background is less smooth than the IRI background but the general shape is similar. The ESR background  $T_e$  is noticeably lower than the IRI  $T_e$  by up to 2000 K in places. This is true for all but one of the cases presented in this paper (the background data from the two methods are within about 800 K for the 23 September 2001 case).

[15] The uncertainty in the ESR mode is calculated using a bootstrap method, this is combined using standard techniques [Squires, 1985] with the uncertainty in the VHF  $T_e$  to give an uncertainty in  $\Delta T_e$ . For the IRI method we assume there is no random error in the model output.

[16] The original method of Aikio *et al.* [2006] used the condition that the  $bT_e$  was located where  $\Delta T_e$  minus the uncertainty in  $\Delta T_e$  crossed zero. Including the subtraction of the uncertainty potentially introduces a bias in the boundary location so we have not included this condition in our calculations. The zero condition assumes that any enhancement of  $T_e$  over the background level indicates the location of the  $bT_e$ ; however, this proved overly restrictive in our testing as

quite often the ESR method  $\Delta T_e$  did not go below zero (i.e., the estimate of the  $T_e$  height profile is not perfect).

[17] The boundary finding method used here is based on the method for locating spectral width boundaries in SuperDARN radar data [see Chisham and Freeman, 2003, section 4; Chisham and Freeman, 2004, section 2]. Prior to looking at each latitude profile separately the  $\Delta T_e$  data is median filtered in the temporal and spatial (both with a filter width of 5) directions. To locate the boundary a threshold temperature,  $T_{et}$ , is chosen and an equatorward search is performed, beginning after the first value below  $T_{et}$ . A boundary is identified when the range gate and two out of three consecutive gates equatorward of it are greater than  $T_{et}$ .

[18] As mentioned earlier the condition used by Aikio *et al.* [2006] where the boundary was identified where  $\Delta T_e$  (minus uncertainty) crossed zero does not work well with the cases shown here implying that the background estimates are not perfect. The question then arises; what threshold should be used? This varies from case to case and between the IRI and ESR methods used in this paper, therefore a range of thresholds have been applied for each case and the best value of  $T_{et}$  chosen. This choice is based on a number of factors, primarily by investigating the distributions of  $\Delta T_e$  in strips of latitude  $2^\circ$  wide poleward and equatorward of the boundary in a similar manner to spectral width boundary investigations by Chisham and Freeman [2004] but also on a visual inspection of the boundary fit to the  $\Delta T_e$  data. This will be described in greater detail with the benefit of an example in section 3.

[19] Once a boundary is identified we use the  $\Delta T_e$  profile and its uncertainty to simulate 100  $\Delta T_e$  profiles within the error range of the data. (We use a normal distribution of random numbers to simulate the profiles, with the mean and standard deviation of the normal distribution set to be the original  $\Delta T_e$  and uncertainty.) We use the boundary finding algorithm to find a boundary in each of the separate 100 simulated  $\Delta T_e$  profiles. The standard deviation of these boundary locations gives us an uncertainty estimate for the boundary location.

## 2.5. DMSP and IMAGE OCB Proxies

[20] The automated boundary identification for DMSP particle data is outlined by *Newell et al.* [1996]. On the nightside, the OCB is given by the b6 boundary [*Chisham et al.*, 2008] which marks the transition from the poleward edge of the subvisual drizzle region to particle fluxes below detectable levels or the first encounter with polar rain.

[21] The FUV imager onboard the IMAGE satellite [*Mende et al.*, 2000a, 2000b] consisted of three detectors observing the aurora with a temporal resolution of 2 min (limited by the spin period of the spacecraft). The Wideband Imaging Camera (WIC) observed emissions in the 140 to 180 nm range from molecular nitrogen caused by electron precipitation. The Spectrographic Imager SI-12 observed the proton aurora at 121.8 nm (doppler shifted Lyman H-alpha) and the SI-13 detector observed the electron aurora at 135.6 nm from oxygen emission. We have used data from the WIC and SI-12 instruments in this study. After 2002 the camera pointing direction became less reliable such that the position of the auroral oval may be offset from its true position by up to 1° of latitude, therefore we have not used IMAGE data in our 2004 case study.

[22] The IMAGE satellite OCB identification method we use is taken from *Boakes et al.* [2008]. Their method determines a latitudinal location for the OCB in each hour of MLT by fitting the sum of a Gaussian (for the auroral oval) and a quadratic (to remove the background) to the latitudinal intensity profile. The peak of the Gaussian function gives the middle of the auroral oval and the OCB is then determined by adding the full width at half maximum to the middle point. The 24 point OCB identified at each satellite data time point has been linearly interpolated both in space and time to match the MLT of Tromsø (MLT  $\approx$  UT + 2.5 h) and the time of the VHF data.

[23] We have used this reasonably simple fitting technique for the IMAGE data but note that the OCB determination may suffer if the background intensity profile takes on a complicated shape or if the auroral oval profile departs from a Gaussian. There are also potential issues if the auroral luminosity is too weak or there is too much dayglow. The OCB identifications were checked manually for accuracy to account for these potential shortfalls in the method.

## 3. Results

### 3.1. The 29 October 2004 Event

[24] As mentioned in section 2.4 determining the most appropriate threshold temperature for the boundary finding algorithm is not simple. In all of the cases in this paper we have based our decision of which  $T_{et}$  to use on three steps: (1) assessing the behavior of  $\Delta T_e$  in strips of latitude either

side of the boundary, (2) looking at which  $T_{et}$  for the IRI method minimizes the median offset of the IRI method boundary to the ESR method boundary chosen by step 1, and (3) a visual inspection of the boundary overlaid on the  $\Delta T_e$  plots.

[25] Figure 2 shows plots for assessing feature 1 of the data for the 29 October 2004 event. This shows the median (Figure 2a) and number of points (Figure 2b) for the ESR method boundary. The distributions from which these statistics come are created by binning all the  $\Delta T_e$  data in 2° ranges poleward and equatorward of the  $T_e$  boundary for the whole interval to be looked at, in this case from 1530 to 2100 UT. Each panel of Figure 2 shows a set of colored lines corresponding to the results of this binning procedure for each temperature threshold applied. The line colors correspond to the color bar on the right. The data point at -1° represents the median or number of points from the 0° to -2° bin etc.

[26] Ideally, a well-identified boundary between the low- and high-temperature regions in the  $\Delta T_e$  data should have a median  $\Delta T_e$  equatorward of the boundary that is significantly higher than poleward of the boundary. Also, poleward of the boundary, the median  $\Delta T_e$  should remain low far from the boundary. The temperature threshold that achieves this best in Figure 2a is 500 K (the darkest red line), this line has a very high median  $\Delta T_e$  equatorward of the boundary and a sharp drop across it which is continued into the 2° to 4° bin. The -300 K line that also shows this type of shape has very few data points associated with it (see Figure 2b) which indicates it is likely to be a poor threshold for the whole time interval. This can be confirmed by visual inspection of the  $\Delta T_e$  data.

[27] We look at the distributions of the latitudinal difference between the IRI and ESR method boundaries to investigate feature 2. To find the best match of the IRI boundary to the ESR method boundary we look at a combination of the median and standard deviation. A good match will have a median close to zero and a small standard deviation. In this event, the best match is for the IRI threshold to be set at 100 K. This ensures the best match between the two boundaries.

[28] Finally we look at how well the boundaries from the thresholds we have identified relate to the  $\Delta T_e$  data; this is presented in Figure 3. Figure 3a shows the  $\Delta T_e$  from the IRI method with the 100 K  $bT_e$  overlaid as the black line. Figure 3c shows the same but for the ESR method with the 500 K  $bT_e$  overlaid. The time resolution of the VHF data used in this interval is 1 min.

[29] These boundaries are shown without the very sharp spikes they have due to noisy data at the northernmost ranges of the  $\Delta T_e$  data. The noisiness in the data at these far ranges is due to the distance from the radar causing a drop in the power of the returned signal. A constant cutoff has been applied and can be varied to suit the data (set at 75.0°N AACGM for this case). The cutoff has been applied after the boundaries have been located, when it is clear to see where the noise has disrupted the boundary.

[30]  $\Delta T_e$  from both methods show a clear, raised  $T_e$  region between 70° and 72° AACGM. This region is cleanly demarcated by the boundary finding algorithm applied in the IRI method for all but the first hour where the enhanced  $T_e$  is not so well defined.

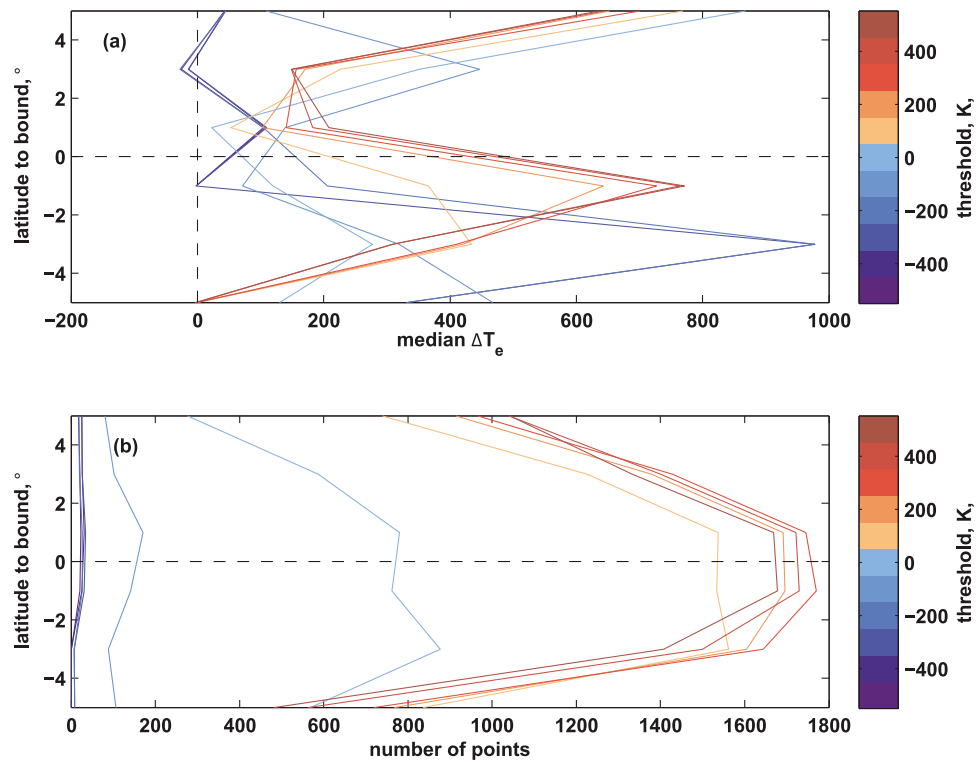


**Figure 2.** Plots showing the median values and number of points for the ESR method. Each line corresponds to a specific threshold temperature shown in the color bar. Each point on a line is the value for the distribution of  $\Delta T_e$  in  $2^\circ$  bins either side of the boundary for that threshold temperature (e.g., the point at  $-1^\circ$  represents the  $0^\circ$ – $2^\circ$  bin).

[31] Figures 3b and 3d show the boundaries from all thresholds from  $-500$  K to  $500$  K in  $100$  K steps for the IRI and ESR methods, respectively. This can be quite useful as a guide to the quality of the boundary found at each time. Where the boundary between hot and cold electrons is steep and sharp, the threshold temperature chosen becomes largely irrelevant; that is, when the edge of the auroral oval is very obvious, the boundary finding works well over a range of threshold temperatures. There is a small caveat to this related to the efficacy of the background  $T_e$  removal. The range of threshold temperatures which give very similar boundaries may not cover the full range of  $-500$  to  $500$  K because the “low”-temperature region may not be sufficiently low to allow the boundary algorithm to find a boundary with lower threshold values. This is particularly the case for the ESR method. For example, Figure 3d shows that for the ESR method the temperature thresholds from  $200$  K and higher work well together but the thresholds below  $200$  K result in very patchy boundaries.

[32] Figure 3e shows the two boundaries compared with each other and also compared to DMSP identifications of the OCB (boundary “b6” from *Newell et al.* [1996]) within  $\pm 15^\circ$  geographic longitude of Tromsø ( $103^\circ$ E). The vertical white on black line is the substorm onset time from the *Frey et al.* [2004] list of substorms (1843 UT). The  $bT_e$  from the two radar methods compare very well, particularly the shape of the boundary motion over time. In the earlier part of the interval the IRI boundary is slightly lower in latitude than the ESR boundary. In the period up to  $\sim 1740$  UT,  $\Delta T_e$  is characterized by narrow, equatorward moving regions of

higher  $T_e$  which cause some difficulties for the boundary algorithm (in terms of which threshold to use) particularly for the IRI method, nor is it very clear from a visual inspection where the OCB proxy should be. After 1740 UT the spread of boundaries with threshold temperature settles down and both the IRI and ESR method produce very similar boundary locations. There is an exception from  $\sim 1840$  to  $1930$  UT where most of the IRI boundaries level out at  $\sim 70^\circ$ ; this does not look like a good boundary identification from inspection of Figure 3a. In this case it seems the statistical method of finding the closest IRI boundary to match the ESR boundary has favored the earlier part of the interval to the detriment of the middle of the interval. Tailoring the boundary threshold temperature to different parts of an interval of data would be potentially beneficial for studies following the motion of the OCB over time. Careful inspection of the initial  $\Delta T_e$  data and how the boundary changes with the threshold temperature should be a good guide to doing this.

[33] A further indication of the quality of the boundary fitting at each threshold temperature can be obtained by looking at the uncertainty in the boundary fit (Figure 4). Each horizontal set of data in this plot shows the uncertainty in finding the boundary at the threshold temperature on the y axis. The color coding shows the standard deviation of the latitudinal variation of the boundary fit in degrees. Figure 4a shows the results for the IRI method fitting, and Figure 4b shows the same for the ESR method. In general, for this interval the higher-threshold values were prone to larger uncertainties with the IRI method although at times the

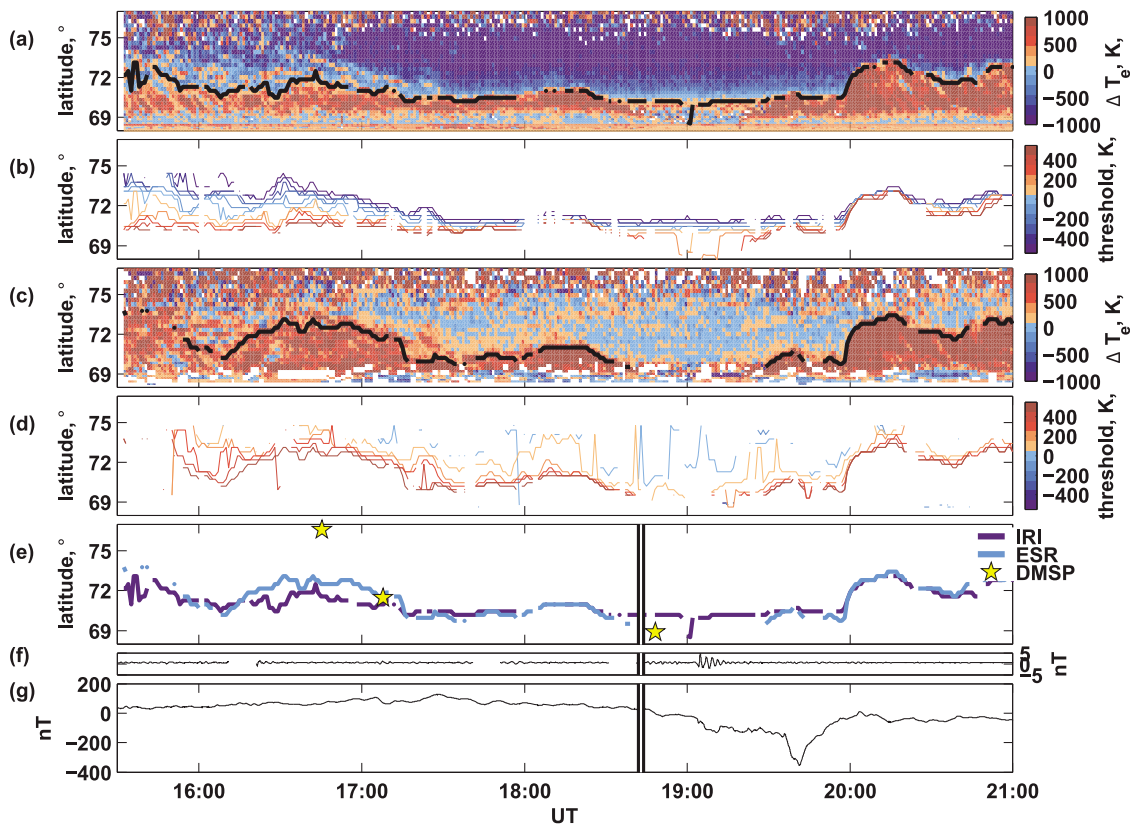


**Figure 3.** For 29 October 2004: (a and c)  $\Delta T_e$  with overlaid  $bT_e$  (black line) from the IRI ( $T_{et} = 100$  K) and ESR ( $T_{et} = 500$  K) methods, respectively; (b and d) the full range of boundaries from  $T_{et}$  ranging from  $-500$  to  $500$  K for the IRI and ESR methods, respectively; (e)  $bT_e$  from the IRI and ESR methods (vertical white on black line is substorm onset time from the *Frey et al.* [2004] list, and yellow stars indicate DMSP b6 identifications); (f) Pi2 filtered (20–200 s)  $H$  component magnetometer data from Lerwick, United Kingdom; (g)  $H$  component magnetometer data from Kilpisjärvi, Finland.

larger uncertainties extend across all threshold temperatures, notably during the interval from  $\sim 1840$  to  $1930$  UT discussed in the previous paragraph as a poorly fitted time. For the ESR method the fitting of the boundary is generally very good, with a small patch of high uncertainties in the same period as the worst fits from the IRI method. It is very noticeable that the ESR method struggles to fit a boundary at all at the most extreme temperature thresholds, this plot shows nicely how this varies over the interval.

[34] The DMSP OCB estimate at  $1707$  UT is in very good agreement with both the IRI  $bT_e$  and ESR  $bT_e$ . The DMSP OCB at  $1848$  UT is in the region where the boundary is fitted poorly by the radar methods, primarily because the OCB is south of the field of view of the radar beam. The DMSP OCB location at  $1645$  UT is very different, some  $3$  to  $4^\circ$  poleward of the two EISCAT derived OCB. The DMSP boundary identifications show a large latitudinal difference between the b5e boundary (poleward boundary of the auroral oval as determined by an abrupt drop in the electron energy flux) and the b6 boundary (poleward boundary of subvisual drizzle roughly adjacent to the oval). The spectrograms are freely available online for the interested reader (<http://sd-www.jhuapl.edu/Aurora/index.html>). This is because there is an extended patch of high electron flux poleward of the “b5e” boundary and also beyond the limit of the oval demarcated by the ion signature in the DMSP

spectrogram. This may mean that the “b6” boundary in this case does not coincide well with the OCB. It may also mean that the  $T_e$  proxy and DMSP ion signature are poor at this time.

[35] Figures 3f and 3g show the Pi2 filtered (20 to 200 s) data from the subauroral magnetometer station at Lerwick in the United Kingdom ( $57.94^\circ\text{N}$ ,  $80.83^\circ\text{E}$ , CGM) and the unfiltered data from the auroral region magnetometer station at Kilpisjärvi in Finland ( $65.92^\circ\text{N}$ ,  $103.6^\circ\text{E}$ , CGM), respectively. According to the *Frey et al.* [2004] list the substorm onset occurs at  $1843$  UT at  $62.46^\circ\text{S}$ ,  $144.5^\circ\text{E}$  geomagnetic coordinates which is approximately  $40^\circ$  east of the VHF beam. This puts EISCAT and the two magnetometers shown here significantly west of the *Frey et al.* [2004] list onset location. Indeed it would appear that the substorm onset in this sector is seen at  $\sim 1905$  UT. This is actually a very large time difference for the onset timings in different MLT regions. The AE indices (provisional AE from World Data Center, Kyoto) at the time show a slight auroral brightening before  $19$  UT but a larger and longer-lived one at a time consistent with the magnetometer data shown in Figure 3.

[36] The LANL (Los Alamos National Laboratory) satellites SOPA (Synchronous Orbit Particle Analyzer) instruments measured a rapid injection of electrons in the energy range  $50$  to  $315$  keV which is a signature of substorm onset at

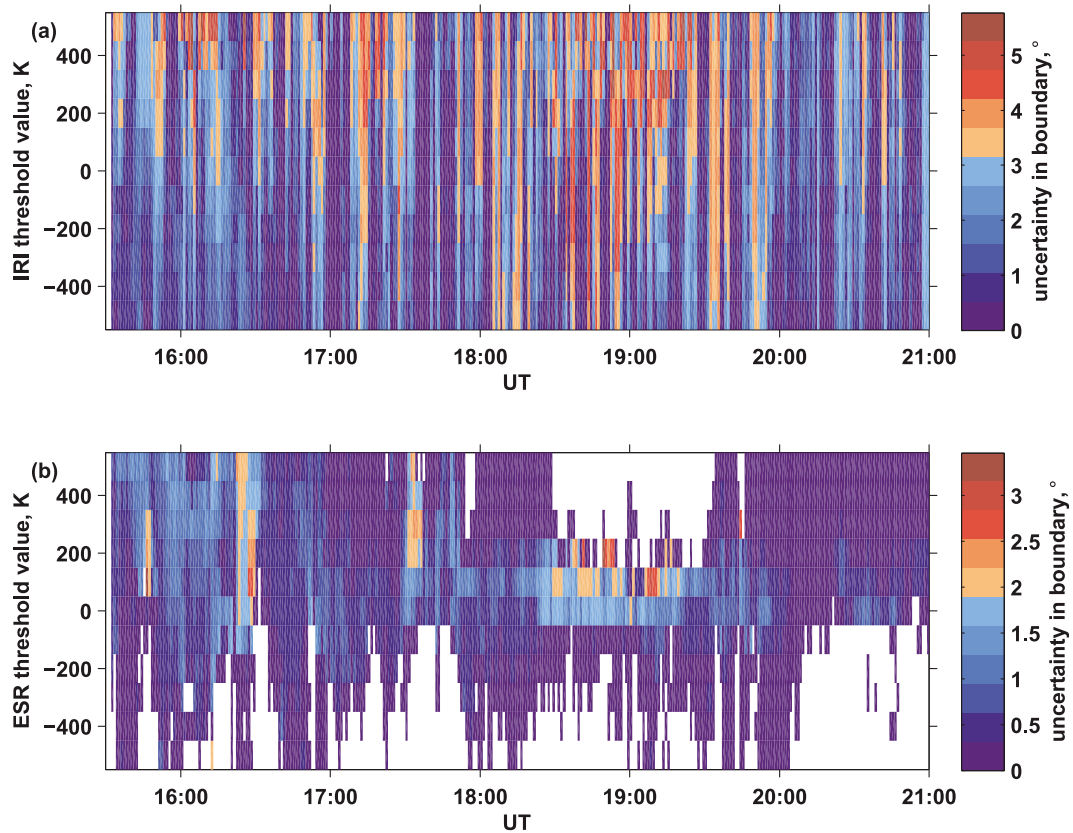


**Figure 4.** For 29 October 2004: plots of the uncertainty in finding a boundary at the different threshold temperature values for (a) the IRI method and (b) the ESR method.

~1840 UT (observed most clearly in the LANL 02A spacecraft data located east of EISCAT). This is in good agreement with the *Frey et al.* [2004] list timing. It seems therefore that the Scandinavian sector sees the second auroral brightening shown in the AE data but misses the original substorm onset.

[37] Presuming that there is an auroral bulge and westward surge from the substorm then the motion of the  $bT_e$  we find in our analysis is consistent with a northward motion of the OCB following the observation of the substorm onset in the Scandinavian sector. Unfortunately in this case, the main burst of the substorm occurs when the OCB proxy for the radar is out of the field of view.

### 3.2. The 23 September 2001 Event

[38] Figure 5 presents the same analysis as in Figure 3 but for 23 September 2001. The enhanced  $T_e$  region is less clear than on 29 October 2004. Nonetheless, the automated boundary finding succeeds in locating a boundary that is reasonably consistent between the two methods albeit with a large amount of variability (Figures 5a and 5c). The threshold temperature identification performed as described for the previous event indicates we should use ESR  $T_{et} = 100$  K and IRI  $T_{et} = 300$  K. In addition to the DMSP boundary identifications and the two  $bT_e$  boundaries in Figure 5e we also show the OCB location estimated from the IMAGE satellite SI-12 data as described in section 1. There is no WIC OCB identification for this interval as

dayglow makes WIC unusable during the event. The EISCAT VHF data is at 1 min resolution.

[39] The spread of the boundaries with threshold temperature in Figures 5b and 5d is very large in this event, a reflection on the lack of clarity of the hot electron temperature region. The uncertainties in the boundary finding also show how difficult it is to find a good boundary, particularly in the first part of this interval (up to ~1810 UT).

[40] The DMSP b6 boundary identified at 1544 UT is from a spectrogram which is a little difficult to interpret so we will not use this for comparison purposes but we have included it for completeness. The DMSP b6 just after 1700 UT matches very well with the ESR and IRI method boundaries. The SI-12 OCB estimation is unfortunately somewhat patchy at this time. At ~1840 UT the OCB convincingly estimated by both DMSP and SI-12 is at the limit of the range of the VHF data and although both IRI and ESR boundaries do match the DMSP b6 location at this time they are not reliable boundaries here. The  $bT_e$  from the chosen IRI threshold at 300 K has reached the edge of the data and is producing a flat line, a clear sign that this is not a good boundary identification and that the OCB proxy for the radar is out of range (or does not exist). The ESR  $bT_e$  is picking up the narrow, transient, equatorward moving patches of enhanced  $\Delta T_e$  at this time. These are not what one needs for a convincing OCB estimation; compare these transients to the end of the 29 October 2004 interval where there is a wide, clear region of enhanced  $\Delta T_e$ .

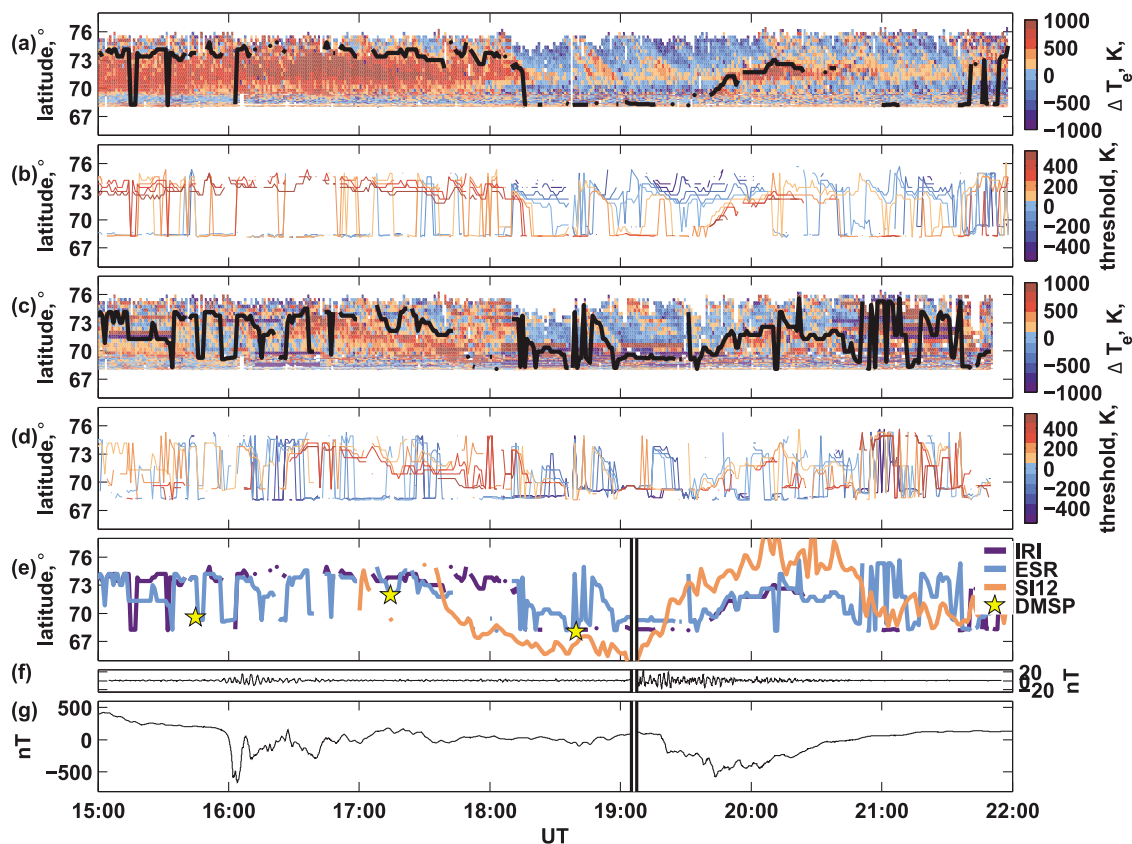


**Figure 5.** For 23 September 2001: (a and c)  $\Delta T_e$  with overlaid  $bT_e$  (black line) from the IRI ( $T_{et} = 300$  K) and ESR ( $T_{et} = 100$  K) methods, respectively; (b and d) the full range of boundaries from  $T_{et}$  ranging from  $-500$  to  $500$  K for the IRI and ESR methods, respectively; (e)  $bT_e$  from the IRI and ESR methods (vertical white on black line is substorm onset time from the *Frey et al.* [2004] list, and yellow stars indicate DMSP b6 identifications); (f) Pi2 filtered (20–200 s)  $H$  component magnetometer data from Lerwick, United Kingdom; (g)  $H$  component magnetometer data from Kilpisjärvi, Finland.

[41] The substorm onset from the *Frey et al.* [2004] list (1906 UT, 58.43°N 90.68°E geomagnetic) is much clearer in this case; the *Frey et al.* [2004] timing and the magnetometer results shown in Figures 5f and 5g match well followed by poleward motion of all the continuous OCB proxies after onset (no nearby DMSP data was available). The *Frey et al.* [2004] onset location is slightly to the west of Scandinavia. The LANL SOPA data show a clear electron injection at  $\sim 1915$  UT, strongest to the east of EISCAT. This coincides with the first sharp decrease in the  $H$  component in Figure 5g. The SI-12 OCB shows a much greater range of latitude change than the IRI or ESR methods due at the latitude extremes to the limitations of the range of the VHF data. The direction of motion of the radar and SI-12 proxies is the same from  $\sim 1930$  to 2030 UT where the IRI boundary stops.

### 3.3. The 29 October 2001 Event

[42] Figure 6 shows the same analysis for the third of our four cases, from 29 October 2001. Similar to the October 2004 case, there is a clear region of  $T_e$  enhancements. The VHF measurements are at 1 min resolution. The boundary threshold investigation results in ESR  $T_{et} = 300$  K and IRI  $T_{et} = 0$  K. A noise cutoff has been applied at 75.0°N AACGM. The boundary identification for both the IRI and

ESR methods works well except for a brief bifurcation of the hot electron region just prior to 1800 UT.

[43] Figures 6b and 6d show much less spread in the boundary with  $T_{et}$  compared to the previous case (September 2001). The uncertainties in the boundary finding are generally higher for higher threshold temperatures for the IRI method with occasional short bursts of high uncertainties at all thresholds. The ESR method uncertainties are much smaller than for IRI in this case but are also worse at higher-threshold temperatures.

[44] The IRI and ESR method boundaries match very well in this case and also with the DMSP b6 identifications and WIC OCB. In particular, the IRI  $bT_e$  is closer to the DMSP and WIC OCB estimates between 1630 and 1700 UT. Visual inspection of the IMAGE WIC identification of the OCB proxy show that it is contaminated by dayglow until  $\sim 1630$  UT which places the OCB artificially high in latitude. This data is not shown in the plot.

[45] This *Frey et al.* [2004] substorm onset (1541 UT, 61.39°N 181.58°E geomagnetic) is probably not a genuine substorm onset. There are no obvious substorm signatures in the magnetometer data in Figures 6f and 6g, although we might not expect them anyway as Scandinavia is  $\sim 6$  h of MLT west of the *Frey et al.* [2004] identified onset location. However, the AE indices show elevated auroral activity

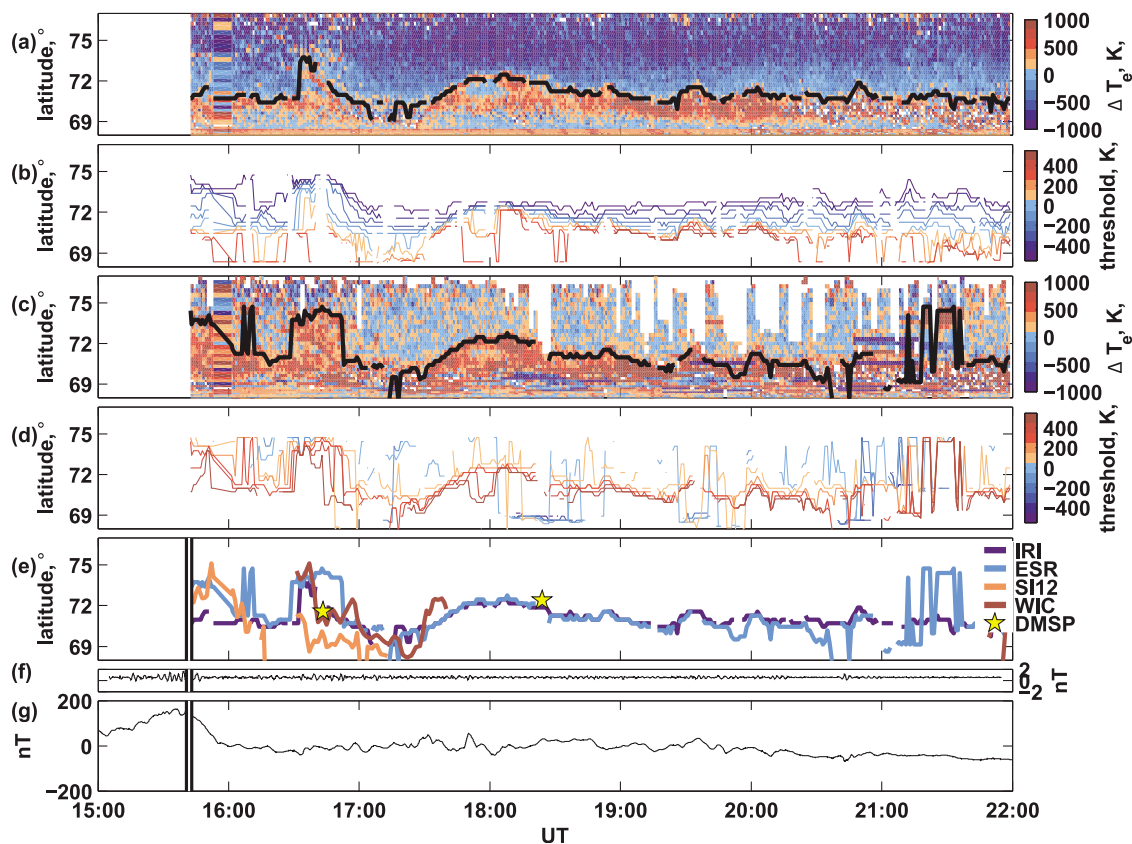


**Figure 6.** For 29 October 2001: (a and c)  $\Delta T_e$  with overlaid  $bT_e$  (black line) from the IRI ( $T_{et} = 0$  K) and ESR ( $T_{et} = 300$  K) methods, respectively; (b and d) the full range of boundaries from  $T_{et}$  ranging from  $-500$  to  $500$  K for the IRI and ESR methods, respectively; (e)  $bT_e$  from the IRI and ESR methods (vertical white on black line is substorm onset time from the *Frey et al.* [2004] list, and yellow stars indicate DMSP b6 identifications); (f) Pi2 filtered (20–200 s)  $H$  component magnetometer data from Lerwick, United Kingdom; (g)  $H$  component magnetometer data from Kilpisjärvi, Finland.

globally but no obvious substorm signature either. Unfortunately there are no LANL data available at this time to check for the onset signature. The motion of the OCB as seen by the proxies plotted in Figure 6e is therefore unlikely to be substorm driven and indeed does not follow the classic polar cap contraction one would expect.

### 3.4. The 13 November 2002 Event

[46] Figure 7 shows the final of our four cases, from 13 November 2002. This is another case where the region of enhanced  $T_e$  is not always obvious from Figures 7a and 7c. The VHF data for this interval has a time resolution of 2 min. The boundary threshold values have been chosen to be: ESR  $T_{et} = 100$  K and IRI  $T_{et} = -500$  K. This interval can be subdivided into two subintervals, before and after  $\sim 1900$  UT. Prior to 1900 UT there are a lot of narrow, transient signatures in  $\Delta T_e$  in both the IRI and ESR plots (Figures 7a and 7c). This leads to a very variable ESR boundary and the IRI boundary in general being much lower in latitude than the ESR  $bT_e$ . It would seem that the OCB proxy is likely to be at or poleward of the top edge of these transient features given the DMSP OCB estimate (Figure 7e). After 1900 UT both radar  $bT_e$  and both IMAGE proxies all agree very well until  $\sim 2115$  UT.

[47] The spread of the boundary locations with threshold temperature is quite large in this case until after 1900 UT when the ESR boundaries for thresholds 100 K and above settle on similar locations. The IRI boundaries are fairly uniformly spread with threshold temperature indicating a very gradual change from hot to cold electrons. The uncertainties in this case are in general less extreme than other cases. The uncertainty in the ESR data is generally worst at the 0 K threshold, but sees bursts of larger uncertainties across all thresholds from 1500 to 1550 UT, 1700 to 1800 UT and 2050 UT to 2140 UT. The IRI uncertainties are in general small, with a short burst of large uncertainties from 2130 to 2200 UT across all threshold values.

[48] At the beginning of this interval the IMAGE and DMSP OCB identifications suggest that the OCB is located out of the range of the VHF measurements (Figure 7e). The DMSP b6 identification just after 1700 UT shows that the EISCAT based OCB proxies are as close to the particle precipitation boundary as the IMAGE satellite OCB (although equatorward rather than poleward of DMSP b6). Visual inspection of the IMAGE SI-12 data shows that before  $\sim 1920$  UT the auroral intensity is very low which causes problems with the boundary fitting technique, this data is not included in the plot. The WIC OCB locations are more reliable than the SI-12 identifications during this

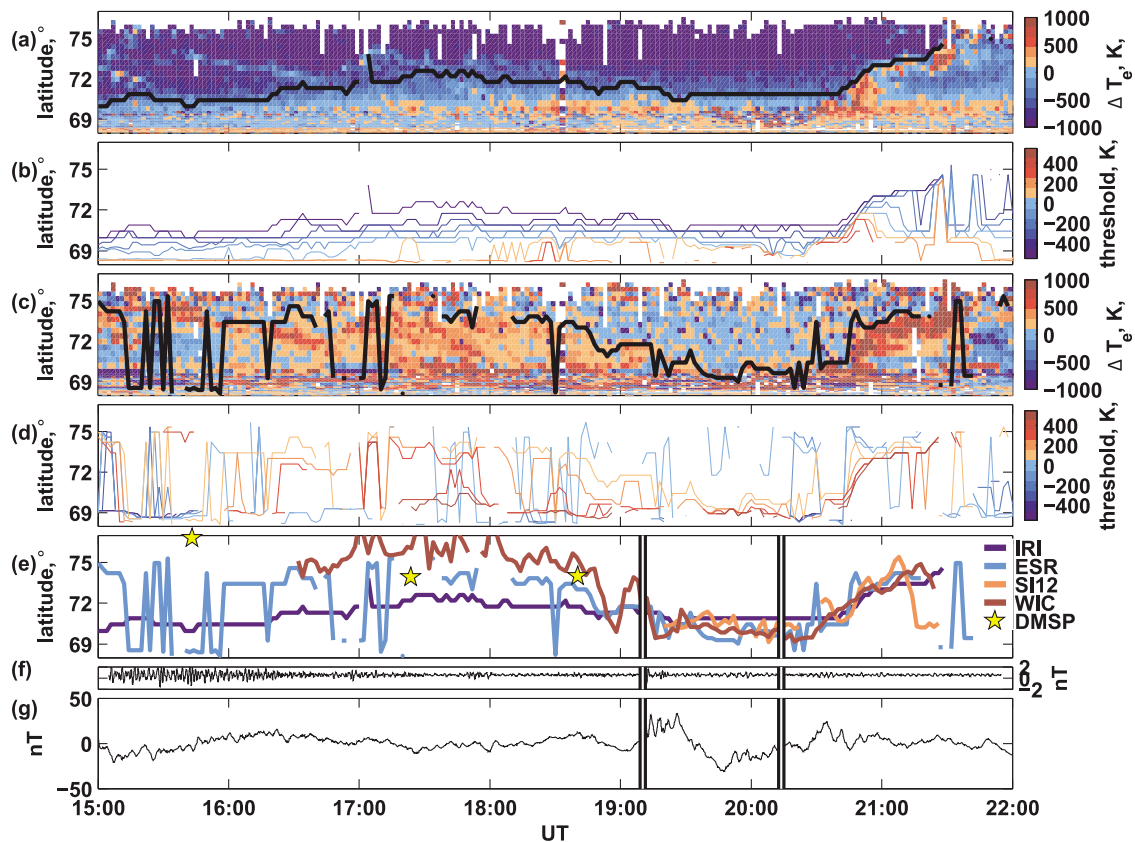


**Figure 7.** For 13 November 2002: (a and c)  $\Delta T_e$  with overlaid  $bT_e$  (black line) from the IRI ( $T_{et} = -500$  K) and ESR ( $T_{et} = 100$  K) methods, respectively; (b and d) the full range of boundaries from  $T_{et}$  ranging from  $-500$  to  $500$  K for the IRI and ESR methods, respectively; (e)  $bT_e$  from the IRI and ESR methods (vertical white on black lines are substorm onset times from the *Frey et al.* [2004] list, and yellow stars indicate DMSP b6 identifications); (f) Pi2 filtered (20–200 s)  $H$  component magnetometer data from Lerwick, United Kingdom; (g)  $H$  component magnetometer data from Kilpisjärvi, Finland.

interval and do show a quite small polar cap. The period between  $\sim 1700$  and  $1800$  UT shows a bulge in the WIC auroral oval between  $\sim 2000$  and  $2400$  MLT. This leads to slightly erratic OCB finding and also the high latitude of the boundary.

[49] This is an interesting pair of substorm identifications from the *Frey et al.* [2004] list (1910 UT,  $65.87^\circ\text{N}$   $125.31^\circ\text{E}$  and 1913 UT  $67.58^\circ\text{N}$   $126.74^\circ\text{E}$  geomagnetic coordinates). First, they are very close together in time meaning at least one of them is unlikely to be a true substorm. There is a very small Pi2 signature (Figure 7f) a few minutes after the first *Frey et al.* [2004] onset time and the Pi2 signature is in turn followed a few minutes later by a small negative bay (Figure 7g). The LANL spacecraft do not observe any electron injections at either *Frey et al.* [2004] onset time, this means that the geostationary footprint probably maps to latitudes equatorward of the substorm. The substorm onset location is placed between 1 and 2 h later in MLT than the EISCAT radar by the *Frey et al.* [2004] identification. There is a marked auroral brightening shown by the AE index between 1900 and 1930 UT. WIC data shows a clear substorm-like brightening at 1910 UT with the later brightening being less distinct. The SI-12 camera observes the first brightening but not the second. Most interesting though is what happens to the OCB between and after the two *Frey*

*et al.* [2004] onset times. The first auroral brightening picked up as an onset by the *Frey et al.* [2004] analysis appears to steady the motion of the OCB proxies and bring all the signatures which can be associated with it into agreement. The second *Frey et al.* [2004] onset marks the time at which the OCB starts to move poleward as would be expected when the nightside reconnection starts to close magnetic flux.

## 4. Discussion

### 4.1. Boundary Thresholds and Boundary Quality

[50] In our investigation of these four intervals we found that identifying an appropriate threshold temperature for the boundary finding algorithm is not simple. As discussed in section 3 we used three steps to identify the thresholds: (1) the behavior of  $\Delta T_e$  in strips of latitude either side of the boundary, (2) looking at which  $T_{et}$  for the IRI method minimizes the median offset with a low standard deviation of the IRI method boundary to the ESR method boundary chosen by step 1, and (3) a visual inspection of the boundary overlaid on the  $\Delta T_e$  plots. Using these steps produces an optimized match between the ESR and IRI boundaries. It is expected that if the IRI method were to be used alone (without the benefit of ESR data) then steps 1 and 3 should

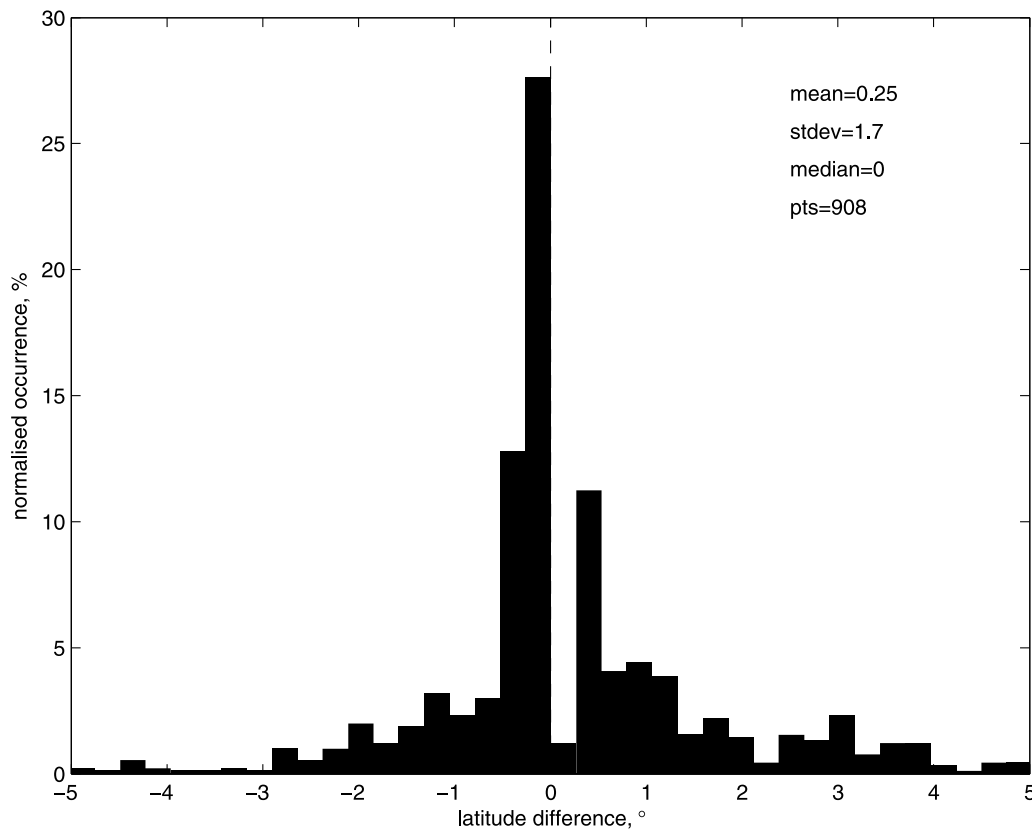


**Figure 8.** Distribution of latitudinal difference (AACGM) between  $bT_e$  from the IRI and ESR methods (ESR minus IRI latitude) for all four cases added together.

provide a good estimate of the best boundary threshold, as long as the following caveats about threshold quality are considered.

[51] We used two main methods to assess the quality and reliability of the boundaries: first the spread of the boundaries as the threshold temperature is varied and secondly the uncertainty in the boundary finding process. Where the OCB proxy is clear there is a sharp, well defined change from a large area of hot electrons to the cold electrons of the polar cap (as in Figure 3a after  $\sim 1740$  UT). With data like this, automated finding of the OCB proxy boundary is easy and the threshold temperature is relatively unimportant. Therefore an investigation of the spread of the boundaries from various thresholds gives an indication of the reliability of the fitting process. We used a range of thresholds from  $-500$  to  $500$  K, but there were times when a subset of the thresholds tested agreed well as lower (or higher) temperature thresholds struggled to fit points at all.

[52] It appears that there is no pair of threshold values from the ESR and IRI methods that will fit all the cases we studied. It is also unfortunately the case that there is no standard relationship between the threshold values from the two methods. This means using the IRI method on its own would probably result in a less accurate OCB proxy; however, the methods applied here to find the best boundary can be adapted to work on the IRI method alone. Most importantly, the boundary threshold where the boundary is well defined is relatively unimportant so using plots such as Figure 3b will help identify good boundary locations.

[53] The other main tool in assessing the reliability of the OCB proxy location is the uncertainty in the boundary location calculated as described in section 2.4. This can be plotted for all thresholds tested as in Figure 4 which gives not only a helpful indication of where the boundary is not well defined, but also shows clearly where the threshold value fails completely to find a boundary (i.e., the blank data points on the plot).

#### 4.2. Comparison of ESR and IRI Methods

[54] The results presented in section 3 indicate a good agreement between the IRI and ESR methods and the satellite OCB proxies. A more detailed comparison of the four events reveals means and medians very close to  $0^\circ$  difference in latitude. This is due at least in part to the optimization of the match between the IRI and ESR boundaries. Figure 8 shows the distribution for all the cases taken together; it has a mean of  $0.25^\circ$  difference (positive means the ESR boundary is poleward of the IRI boundary on average) and a standard deviation of  $1.7^\circ$ .

[55] Looking at the statistics in terms of these distributions hides any local time dependence of the relationship between the two boundary methods, but plotting the latitude differences as time series (not shown) reveals there is no particular dependence on the time of day. Figure 9 shows the latitudinal difference from the two boundaries (ESR - IRI) plotted against the mean boundary latitude for the four cases. The diagonal lines show the theoretical limits beyond which no scatter is possible. It can be seen from these plots

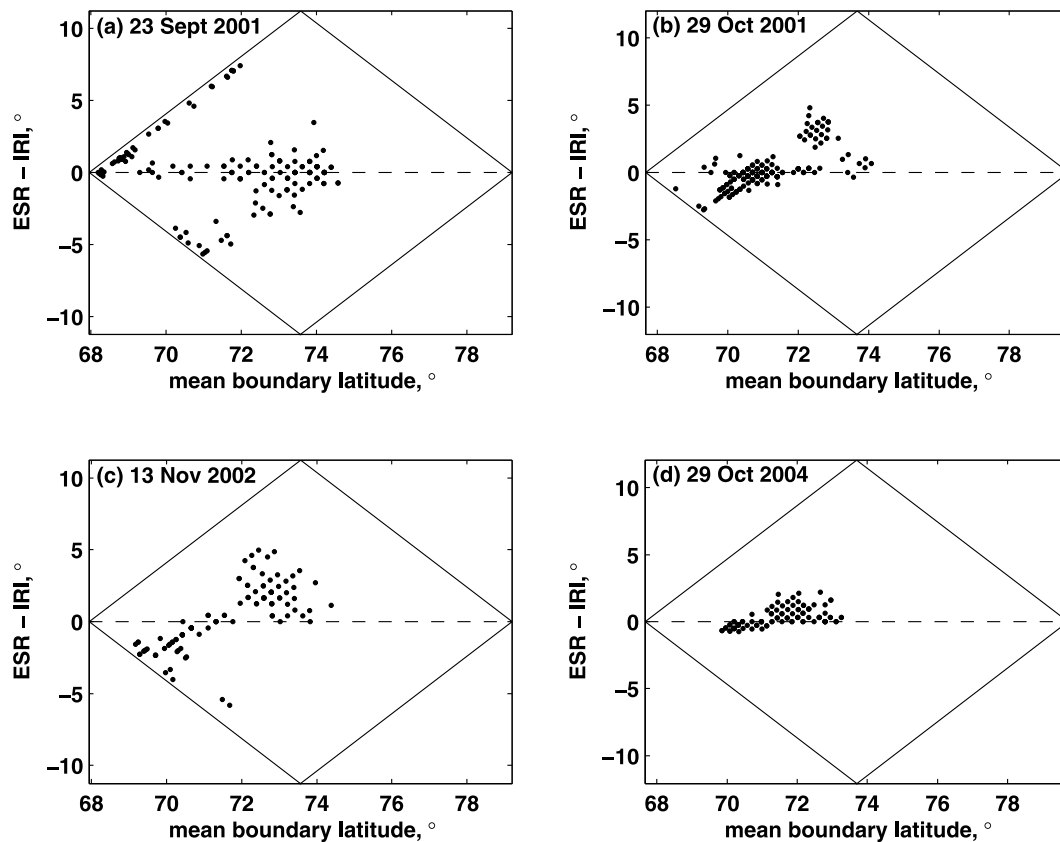


**Figure 9.** Plots of difference in boundary latitude (ESR minus IRI) against mean boundary latitude for ESR and IRI methods. Panels show results from each case. The diagonal lines show the theoretical limits beyond which no points will be seen.

that there is a slight tendency for the IRI boundary to be at higher latitudes than the ESR boundary when the mean boundary latitude is lower. This is most likely a result of the differences in the background  $T_e$  subtracted from the VHF data in the two different methods.

[56] The  $\Delta T_e$  data from 23 September 2001 does not immediately appear to be very different in character from the other event without a clear enhancement in  $\Delta T_e$  (13 November 2002). The general geomagnetic activity is not so very different in the three other cases shown here; however, the 23 September 2001 event appears to be in the main phase of a very short geomagnetic storm or ring current enhancement (SYM-H varies between  $-50$  and  $-100$  nT, Kp varies between 4+ and 6, data sourced from the World Data Center, Kyoto). The October 2001 event appears to be in a mildly active but fairly steady situation, (SYM-H is steady at  $\sim -50$  nT, Kp is between 3 and 3-). The November 2002 event is fairly quiet and steady (SYM-H is  $\sim -20$  nT, Kp varies between 3 and 2-). The October 2004 event is again quiet, but has a more variable SYM-H (between  $\sim -10$  and  $-30$  nT, Kp varies between 3 and 2-). As mentioned in section 2.2 the IRI-2007 results were substantially closer in value to the  $T_e$  height profile background generated from the ESR field aligned data in the September 2001 case. One possible explanation therefore is that the September 2001 case has a background much closer to that for the rest of the month it comes from such that the monthly averages produced by the IRI-2007 model are much closer to the actual

values on that specific day. Conversely, the other three cases were during more unusual conditions for their respective months.

#### 4.3. Comparison to Other OCB Proxies and Substorm Response

[57] As stated earlier, although the ESR and IRI methods do vary in relation to each other it is not immediately obvious if either of them perform better in terms of locating the actual OCB. To attempt to estimate this we have compared the two boundaries to satellite data from both DMSP particle data and the IMAGE UV aurora OCB proxies. It is normally assumed that the DMSP particle boundary b6 is the most accurate locator for the nightside OCB [Chisham *et al.*, 2008]; however, it is hard to produce any statistical comparison from our four events with the DMSP data since there are only a few instances of nearby crossings to the EISCAT radar system. From a qualitative visual inspection of the plots in Figures 3, 5, 6, and 7 neither the IRI or ESR method is clearly better in terms of the DMSP boundary identifications.

[58] To try and quantify the accuracy of the two EISCAT based methods we compare these to the IMAGE satellite OCB proxies. The accuracy of the IMAGE OCB proxies has been determined by Boakes *et al.* [2008] using DMSP particle boundaries. They showed some MLT dependence of the offset between IMAGE OCB latitudes and DMSP OCB identifications. This also varied with the IMAGE camera

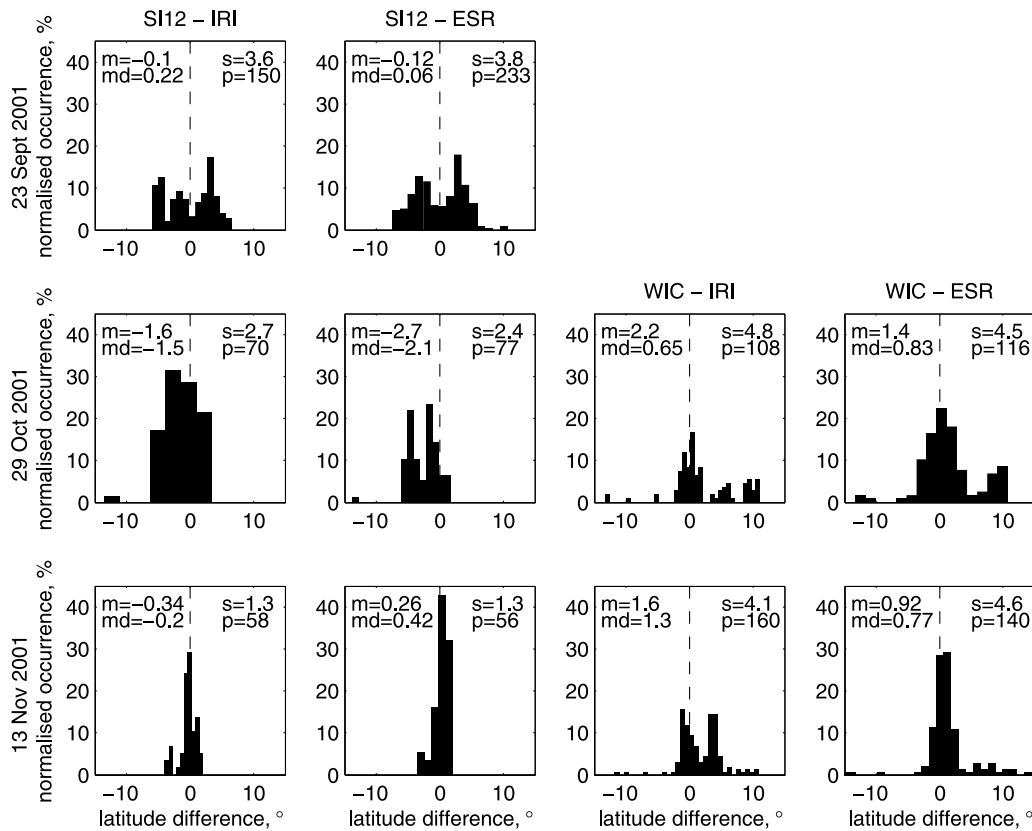


**Figure 10.** Distributions of IMAGE satellite OCB latitudes minus the two different  $bT_e$  methods: m, mean; md, median; s, standard deviation; p, number of points of each distribution. Each row is from a different case. There is no WIC OCB data for 23 September 2001.

being used to generate the OCB estimates. In the 17 to 24 MLT sector that this paper is concerned with, the statistical comparison from *Boakes et al.* [2008] shows that the SI-12 OCB is about  $1^\circ$  equatorward of the DMSP OCB and the WIC OCB is about  $1^\circ$  poleward. This data only goes to  $\sim 21$  MLT due to the orbits of the DMSP spacecraft.

[59] Figure 10 shows the individual comparisons from the three cases where we have IMAGE satellite data separated into four categories: SI-12 - IRI, SI-12 - ESR, WIC - IRI and WIC - ESR. The “m,” “md,” “s,” and “p” give the mean, median, standard deviation and number of points of the distributions, respectively. The number of bins in each histogram has been optimized using the method by *Shimazaki and Shinomoto* [2007]. The OCB estimates from the IMAGE satellite data that have been identified as bad data (see section 3) are not included in these distributions (i.e., WIC data from 1500 to 1630 UT on 29 October 2001 and SI-12 data from 1500 to 1920 UT on 13 November 2002). Overall the comparison to IMAGE OCB locations of the IRI and ESR methods is favorable with means ranging from as small as  $-0.1^\circ$  to as large as  $-2.7^\circ$ . Figure 10 also shows that neither the IRI nor the ESR method is particularly closer to the IMAGE OCB method. Which EISCAT method is closer to the IMAGE satellite method varies from case to case.

[60] We chose our events based on the substorms identified by *Frey et al.* [2004] and some of these were found to be not true onsets when compared to other well known substorm identification methods. Nonetheless, where sub-

storms were identified in our events all of the time-continuous OCB locating methods employed (the IRI, ESR and IMAGE methods) show the expected response to substorm onsets, namely a contraction of the polar cap following substorm onset. The analysis of our cases would seem to indicate that using the IRI-2007 model as a background  $T_e$  measure to monitor the OCB during substorms is a potentially good substitute for ESR data if none is available.

## 5. Conclusions

[61] We have shown that through careful inspection of the data, the IRI-2007 model can be used instead of ESR data as a background  $T_e$  height profile. This background height dependence can then be removed from low-elevation  $T_e$  variations (EISCAT VHF data in the cases shown here) leaving a clearer latitude dependence of  $T_e$  from which an OCB proxy can be identified. We have described how to obtain the most appropriate boundary threshold temperature and determine the subsequent boundary reliability.

[62] The IRI method works well in comparison to the ESR method with a mean latitude difference of  $0.25^\circ$ . There is a slight dependence of latitude difference between the ESR and IRI methods with mean latitude of the two boundaries, most likely due to the differences between the ESR and IRI electron temperature profiles.

[63] A comparison of both the IRI and ESR methods to known proxies for the OCB shows that neither method is

closer to the DMSP OCB proxy than the other in a general sense but that this varies from case to case. The comparison to the IMAGE satellite OCB identifications using the method of Boakes *et al.* [2008] showed a variation in the magnitude of the mean latitude difference between the IRI/ESR methods and the IMAGE OCB locations of between 0.1 and 2.7°.

[64] Overall, the IRI method seems to be very promising as a replacement for ESR data when they are not available. This is not to say that the IRI-2007 model does a good job of modeling the  $T_e$  at these auroral latitudes, indeed we saw that the values can be out by as much as 2000 K, but rather that it does a sufficiently good job to allow the boundary finding algorithm to work.

[65] **Acknowledgments.** E.E.W., J.A.W., A.J.K., and A.S. are all supported by STFC, United Kingdom. We would like to thank all those involved in the IMAGE satellite project for their data. The DMSP particle detectors were designed by Dave Hardy of AFRL, and data were obtained from JHU/APL. We thank the institutes that maintain the IMAGE Magnetometer Array and those that maintain the SAMNET and BGS Magnetometers. EISCAT is an international association supported by China (CRIRP), Finland (SA), Japan (STEL and NIPR), Germany (DFG), Norway (NFR), Sweden (VR), and the United Kingdom (NERC).

[66] Robert Lysak thanks Gareth Chisham and Keisuke Hosokawa for their assistance in evaluating this paper.

## References

- Aikio, A. T., T. Pitkanen, A. Kozlovsky, and O. Amm (2006), Method to locate the polar cap boundary in the nightside ionosphere and application to a substorm event, *Ann. Geophys.*, *24*(7), 1905–1917.
- Aikio, A. T., T. Pitkanen, D. Fontaine, I. Dandouras, O. Amm, A. Kozlovsky, A. Vaivadas, and A. Fazakerley (2008), EISCAT and Cluster observations in the vicinity of the dynamical polar cap boundary, *Ann. Geophys.*, *26*(1), 87–105.
- Baker, K., and S. Wing (1989), A new magnetic coordinate system for conjugate studies at high latitudes, *J. Geophys. Res.*, *94*(A7), 9139–9143.
- Bilitza, D., and B. W. Reinisch (2008), International reference ionosphere 2007: Improvements and new parameters, *Adv. Space Res.*, *42*(4), 599–609, doi:10.1016/j.asr.2007.07.048.
- Blanchard, G. T., J. C. Lyons, L. R. Samson, and F. J. Rich (1995), Locating the polar-cap boundary from observations of 6300 Angstrom auroral emission, *J. Geophys. Res.*, *100*(A5), 7855–7862.
- Blanchard, G., L. Lyons, and O. de la Beaujardiere (1997), Magnetotail reconnection rate during magnetospheric substorms, *J. Geophys. Res.*, *102*(A11), 24,303–24,312.
- Boakes, P. D., S. E. Milan, G. A. Abel, M. P. Freeman, G. Chisham, B. Hubert, and T. Sotirelis (2008), On the use of IMAGE FUV for estimating the latitude of the open/closed magnetic field line boundary in the ionosphere, *Ann. Geophys.*, *26*(9), 2759–2769.
- Chisham, G., and M. Freeman (2003), A technique for accurately determining the cusp-region polar cap boundary using SuperDARN HF radar measurements, *Ann. Geophys.*, *21*(4), 983–996.
- Chisham, G., and M. Freeman (2004), An investigation of latitudinal transitions in the SuperDARN Doppler spectral width parameter at different magnetic local times, *Ann. Geophys.*, *22*(4), 1187–1202.
- Chisham, G., M. Freeman, M. Lam, G. Abel, T. Sotirelis, R. Greenwald, and M. Lester (2005), A statistical comparison of SuperDARN spectral width boundaries and DMSP particle precipitation boundaries in the afternoon sector ionosphere, *Ann. Geophys.*, *23*(12), 3645–3654.
- Chisham, G., et al. (2008), Remote sensing of the spatial and temporal structure of magnetopause and magnetotail reconnection from the ionosphere, *Rev. Geophys.*, *46*, RG1004, doi:10.1029/2007RG000223.
- de la Beaujardiere, O., L. R. Lyons, and E. Friis-Christensen (1991), Sondrestrom radar measurements of the reconnection electric field, *J. Geophys. Res.*, *96*(A8), 13,907–13,912.
- Doe, R., J. Vickrey, E. Weber, H. Gallagher, and S. Mende (1997), Ground-based signatures for the nightside polar cap boundary, *J. Geophys. Res.*, *102*(A9), 19,989–20,005.
- Frey, H., S. Mende, V. Angelopoulos, and E. Donovan (2004), Substorm onset observations by IMAGE-FUV, *J. Geophys. Res.*, *109*, A10304, doi:10.1029/2004JA010607.
- Hubert, B., A. T. Aikio, O. Amm, T. Pitkanen, K. Kauristie, S. E. Milan, S. W. H. Cowley, and J.-C. Gerard (2010), Comparison of the open-closed field line boundary location inferred using IMAGE-FUV S112 images and EISCAT radar observations, *Ann. Geophys.*, *28*(4), 883–892.
- Mende, S. B., et al. (2000a), Far ultraviolet imaging from the IMAGE spacecraft. 1. System design, *Space Sci. Rev.*, *91*(1–2), 243–270.
- Mende, S. B., et al. (2000b), Far ultraviolet imaging from the IMAGE spacecraft. 2. Wideband FUV imaging, *Space Sci. Rev.*, *91*(1–2), 271–285.
- Newell, P., Y. Feldstein, Y. Galperin, and C. Meng (1996), Morphology of nightside precipitation, *J. Geophys. Res.*, *101*(A5), 10,737–10,748.
- Østgaard, N., J. Moen, S. Mende, H. Frey, T. Immel, P. Gallop, K. Oksavik, and M. Fujimoto (2005), Estimates of magnetotail reconnection rate based on IMAGE FUV and EISCAT measurements, *Ann. Geophys.*, *23*(1), 123–134.
- Shimazaki, H., and S. Shinomoto (2007), A recipe for optimizing a time-histogram, *Adv. Neural Inf. Process. Syst.*, *19*, 1289–1296.
- Squires, G. L. (1985), *Practical Physics*, Cambridge Univ. Press, Cambridge, U.K.
- Wild, J., S. Milan, C. Owen, J. Bosqued, M. Lester, D. Wright, H. Frey, C. Carlson, A. Fazakerley, and H. Reme (2004), The location of the open-closed magnetic field line boundary in the dawn sector auroral ionosphere, *Ann. Geophys.*, *22*(10), 3625–3639.
- Woodfield, E., J. Davies, P. Eglitis, and M. Lester (2002), A case study of HF radar spectral width in the post midnight magnetic local time sector and its relationship to the polar cap boundary, *Ann. Geophys.*, *20*(4), 501–509.

A. J. Kavanagh, A. Senior, J. A. Wild, and E. E. Woodfield, Physics Department, Lancaster University, Lancaster LA1 4YB, UK. (emma.woodfield@lancaster.ac.uk)

S. E. Milan, Department of Physics and Astronomy, University of Leicester, University Road, Leicester LE1 7RH, UK.